Engineering 6 (2020) 927–935

Contents lists available at ScienceDirect

Engineering

journal homepage: www.elsevier.com/locate/eng

Research
Geodesy and Survey Engineering—Article

Precise Three-Dimensional Deformation Retrieval in Large and Complex Deformation Areas via Integration of Offset-Based Unwrapping and Improved Multiple-Aperture SAR Interferometry: Application to the 2016 Kumamoto Earthquake

Won-Kyung Baek, Hyung-Sup Jung *

Department of Geoinformatics, University of Seoul, Seoul 02504, Republic of Korea

ARTICLE INFO

Article history:
Received 20 October 2018
Revised 28 March 2020
Accepted 29 June 2020
Available online 3 July 2020

Keywords:
Synthetic aperture radar (SAR)
Conventional SAR interferometry (InSAR)
Multiple-aperture SAR interferometry (MAI)
ALOS-2 PALSAR-2
3D deformation retrieval
2016 Kumamoto earthquake

ABSTRACT

Conventional synthetic aperture radar (SAR) interferometry (InSAR) has been successfully used to precisely measure surface deformation in the line-of-sight (LOS) direction, while multiple-aperture SAR interferometry (MAI) has provided precise surface deformation in the along-track (AT) direction. Integration of the InSAR and MAI methods enables precise measurement of the two-dimensional (2D) deformation from an interferometric pair; recently, the integration of ascending and descending pairs has allowed the observation of precise three-dimensional (3D) deformation. Precise 3D deformation measurement has been applied to better understand geological events such as earthquakes and volcanic eruptions. The surface deformation related to the 2016 Kumamoto earthquake was large and complex near the fault line; hence, precise 3D deformation retrieval had not yet been attempted. The objectives of this study were to ① perform a feasibility test of precise 3D deformation retrieval in large and complex deformation areas through the integration of offset-based unwrapped and improved multiple-aperture SAR interferograms and ② observe the 3D deformation field related to the 2016 Kumamoto earthquake, even near the fault lines. Two ascending pairs and one descending the Advanced Land Observing Satellite-2 (ALOS-2) Phased Array-type L-band Synthetic Aperture Radar-2 (PALSAR-2) pair were used for the 3D deformation retrieval. Eleven *in situ* Global Positioning System (GPS) measurements were used to validate the 3D deformation measurement accuracy. The achieved accuracy was approximately 2.96, 3.75, and 2.86 cm in the east, north, and up directions, respectively. The results show the feasibility of precise 3D deformation measured through the integration of the improved methods, even in a case of large and complex deformation.

1. Introduction

Conventional synthetic aperture radar (SAR) interferometry (InSAR) is a powerful tool that can measure precise surface deformation over a large area of greater than 1000 km^2. The technique has been successfully applied to earthquake deformation [1–6], volcanic deformation [7–11], glacier movement [12–15], land subsidence [16–19], temporary and seasonal wetland water-level variation [20,21], and so forth. However, because the InSAR method can only observe one-dimensional (1D) deformation in the satellite's line-of-sight (LOS) direction, along-track (AT) deformation measurement is nearly impossible using this method.

However, multiple-aperture SAR interferometry (MAI) was proposed by Bechor and Zebker [22] and further improved by Jung et al. [23–26]. The MAI method enables precise measurement of 1D surface deformation in the AT direction. This method overcomes the limitation of the InSAR method. MAI processing includes the following steps: ① generation of a forward-looking differential interferogram using the forward-looking Doppler spectrum; ② generation of backward-looking differential interferograms using the backward-looking Doppler spectrum; and ③ creation of an MAI interferogram by estimating the phase difference of the two interferograms. It is well known that MAI performance is several times better than that of azimuth offset tracking [22–26].

* Corresponding author.
E-mail address: hsjung@uos.ac.kr (H.-S. Jung).

https://doi.org/10.1016/j.eng.2020.06.012

Two-dimensional (2D) surface deformation can be precisely measured from one interferometric pair using InSAR and MAI integration. Moreover, the integration enables the observation of three-dimensional (3D) deformation using the ascending and descending interferometric pairs. The feasibility of the SuperSAR multi-azimuth SAR system has been tested for precise 3D deformation measurement [27]. 3D retrieval has been widely used to measure volcanic deformation [8,9,28–32], co-seismic deformation [4,5,33–38], glacier movement [39,40], and more. The archived 3D measurement performance using an X-band Constellation of Small Satellites for the Mediterranean Basin Observation-SkyMed (COSMO-SkyMed) InSAR and MAI integration method in the east, north, and up directions was approximately 0.86, 1.04, and 0.55 cm, respectively [29]. However, 3D deformation retrieval remains challenging in large and complex deformation areas due to MAI coherence loss and InSAR phase unwrapping error.

Recently, Jung et al. [26] introduced forward- and backward-looking residual interferograms to reduce the phase noise level. As a result, the method largely enhanced MAI coherence, particularly for decorrelated areas because of large and complex deformation. Baek et al. [41] introduced the multi-kernel offset tracking method [13,15,42] to minimize the phase unwrapping error in high steep deformation areas. They showed that the Advanced Land Observing Satellite-2 (ALOS-2) Phased Array-type L-band Synthetic Aperture Radar-2 (PALSAR-2) offset maps estimated using the multi-kernel offset tracking method are as precise as those used to minimize the phase unwrapping error. Because InSAR measurement is not available in large and complex deformation areas but the offset map is valid, it is possible to measure the LOS deformation using the multi-kernel offset tracking method. The integration of the improved InSAR and MAI measurements enables precise mapping of 3D deformation even in areas that are decorrelated because of large and complex surface deformation. However, this method of integration had never been applied to generate a 3D deformation map.

In this study, we show that the integration of the offset-based unwrapped InSAR [41] and improved MAI methods [26] enables observation of the 3D deformation field deformation even in areas that are decorrelated because of large and complex surface deformation. The 2016 Kumamoto earthquake 3D deformation field was observed by integrating the improved InSAR and MAI methods. The earthquake struck Kumamoto, Japan, on 14 April 2016 and surface deformation occurred along northeast–southwest (NE–SW)-trending strike-slip faults. The earthquake-related surface deformation was large and complex near the fault line; hence, precise 3D surface deformation retrieval had not yet been attempted using InSAR and MAI integration. For this study, two ascending pairs and one descending ALOS-2 PALSAR-2 interferometric pair were acquired and processed to retrieve the 2016 Kumamoto earthquake 3D deformation field. Eleven Global Positioning System (GPS) station measurements were used to evaluate the achieved performance of the 3D deformation measurement via the improved InSAR and MAI integration.

2. Study area and data

Two earthquakes of moment magnitude Mw 6.2 and Mw 6.0 struck Kumamoto, Japan, on 14 April 2016; more than 140 aftershocks were observed following the main events. Subsequently, the main shock of Mw 7.0 occurred after approximately 28 h. It has been reported that the 2016 Kumamoto earthquake resulted in large and complex deformation along NE–SW-trending strike-slip faults [38,43,44]. Subsidence of approximately 2.1 m was observed near the fault zone and uplift of approximately 0.3 m was measured. Eastward deformation of approximately 2.0 m was also observed [40]. Therefore, the surface deformation related to the 2016 Kumamoto earthquake was large and complex, particularly near the fault zone.

Two ascending pairs and one descending ALOS-2 PALSAR-2 co-seismic interferometric pair were used for this study. One of the ascending pairs was obtained on 19 November 2015 and 16 June 2016 (20151119_20160616), and the other was acquired on 11 February 2016 and 2 June 2016 (20160211_20160602). The descending pair was obtained on 7 March 2016 and 18 April 2016 (20160307_20160418). The perpendicular baselines of the three pairs were as short as 30, −74, and −121 m and the temporal baselines were 210, 140, and 42 days. Table 1 summarizes the interferometric parameters of the co-seismic interferometric pairs used for this study. Fig. 1 shows a shaded relief map of Kumamoto, Japan, including the boundaries of the two ascending pairs and the one descending interferometric pair. As shown in Fig. 1, GPS station measurements, marked by solid triangles, were used to evaluate the achieved accuracy of the measured 3D deformation.

3. Method

In large and complex deformation areas, 3D deformation retrieval is difficult because of the unwrapping error in InSAR processing and the coherence loss in MAI processing. An offset-based phase unwrapping has been successfully applied to the ALOS-2 PALSAR-2 interferogram [41]. Thus, it has been reported that InSAR-measured LOS deformation can be observed even in large and complex deformation areas through the improved InSAR method proposed in Ref. [41], which includes offset-based phase unwrapping. Meanwhile, the MAI processing method has been developed to mitigate the MAI coherence reduction since it was first proposed by Bechor and Zebker [22]. Recently, the MAI processor was improved by calculating MAI interferograms via residual forward- and backward-looking interferograms [26]. The improved MAI processor, as discussed in Ref. [26], is effective in mitigating the MAI coherence loss. Therefore, precise MAI-measured AT deformation can be acquired even in a large and complex deformation area [26]. These technical improvements enable InSAR and MAI integration to be applied to the precise measurement of large and complex 3D deformation. Fig. 2 shows a detailed workflow of the improved InSAR and MAI integration for 3D deformation retrieval. A precise 2D deformation map can be generated using the InSAR and MAI processors improved by Baek et al. [41] and Jung et al. [26]. Given both the ascending and descending acquisitions, a 3D deformation map can be precisely created from the ascending and descending 2D deformation maps, as shown in Fig. 2 [26,41].

3.1. Short description of improved InSAR method

The improved InSAR method has five main steps: ① wrapped differential interferogram creation; ② range offset image calculation and filtering; ③ residual interferogram generation by subtracting

Table 1
Co-seismic interferometric pairs acquired from ALOS-2 PALSAR-2 data in the ascending and descending orbits.

Orbit	Master	Slave	Perpendicular baseline (m)	Temporal baseline (d)
Ascending	19 November 2015	16 June 2016	30	210
Ascending	11 February 2016	2 June 2016	−74	140
Descending	7 March 2016	18 April 2016	−121	42

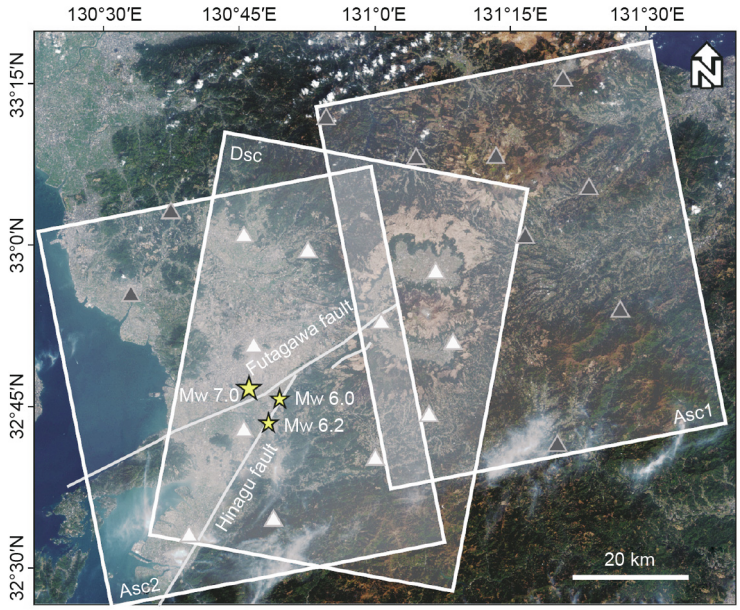

Fig. 1. RGB map (Sentinel-2) of Kumamoto city, Japan, including the boundaries of two ascending and one descending interferometric pairs. The grey lines are ruptures and the yellow stars denote the epicenters of the 2016 Kumamoto earthquake. The white and black triangles indicate the location of the GPS station. Among them, the white triangles were used for validating 3D measurements. The labels "asc1" and "asc2" indicate the interferometric pairs of 20151119_20160616 and 20160211_20160602, respectively, and "dsc" refers to the 20160307_20160418 interferometric pair.

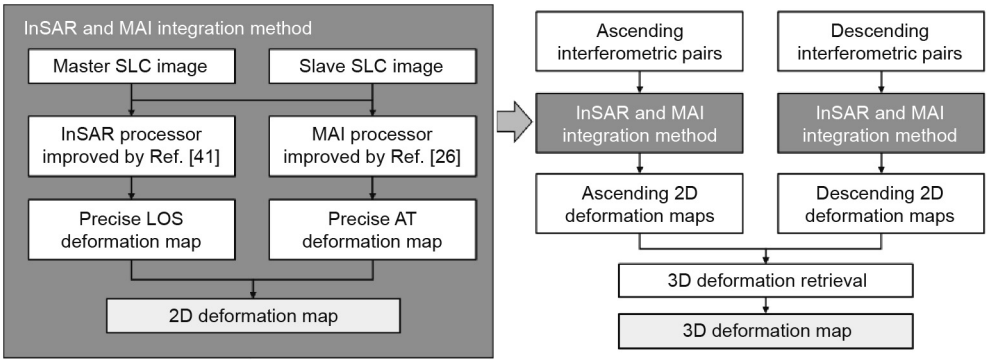

Fig. 2. Detailed workflow for 3D deformation retrieval. SLC: single-look complex.

the filtered range offset image from the wrapped differential interferogram; ④ unwrapped residual interferogram generation; and ⑤ unwrapped differential interferogram creation by summing the unwrapped residual phase and filtered range offset. More details for the process can be found in Ref. [41]. In this InSAR method, the generation of a valid residual interferogram is the key. Usually, it is nearly impossible to generate a valid residual interferogram because the accuracy in the offset method is much lower than the accuracy in the InSAR method. However, this limitation can be overcome by using an ALOS-2 PALSAR-2 interferometric pair and by applying an improved offset tracking method using multiple kernels to the pair [41,42]. The offset tracking performance of the ALOS-2 PALSAR-2 interferometric pair is high due to its higher spatial resolution and improved offset tracking measurement [13,41,42]. This InSAR method makes it possible to measure precise LOS deformation even in large and complex deformation areas.

3.2. Short description of the improved MAI method

The improved MAI method mainly consists of five steps: ① creating three single-look complex (SLC) images via band-pass filtering using full-aperture and forward- and backward-aperture bandwidths for master and slave images, respectively; ② generating three differential interferograms from the three SLC master and slave images; ③ creating two residual interferograms by subtracting the full-aperture differential phase from the forward- and backward-aperture differential phases; ④ creating an MAI interferogram by calculating the phase difference between the two residual interferograms; and ⑤ correcting the residual phases, which includes the topographic and flat-Earth phase corrections, and adaptive filtering of the MAI interferogram. During the first step, the three SLC images must have the same image position, which is achieved by applying the same range cell migration correction. During the second step, the co-registration parameters are estimated by using the full-aperture interferometric pair and then applied to the three interferometric pairs. During the third step, the full-aperture differential interferogram should be hard-filtered by using an adaptive filter such as the Goldstein filter. Hard-filtering can be performed by iteratively applying filters with large window kernel sizes. It is better if the two residual interferograms are lightly filtered before the phase difference calculation during the fourth step. More details of the processing can be found

in Ref. [26]. In MAI processing, it is key for the MAI interferogram to be generated from two residual interferograms. Importantly, the hard-filtered full-aperture differential interferogram should be carefully generated because it is assumed to be a noise-free interferogram. To generate a better hard-filtered interferogram, the small kernel size of 8 × 8 or 16 × 16 pixels can be iteratively applied to the adaptive filter. This MAI method permits the precise measurement of AT deformation even in large and complex deformation areas.

3.3. 3D deformation retrieval

The 3D deformation can be retrieved by combining the ascending and descending 2D deformation measurements. The deformation vector ($\boldsymbol{r}$) can be defined by using the ascending and descending InSAR deformations as well as the ascending and descending MAI deformations, as provided by Refs. [3,8,43], as follows:

$$\boldsymbol{r} = U \cdot \boldsymbol{d} \tag{1}$$

where $\boldsymbol{d}$ is the 3D surface deformation vector and U can be defined as follows:

$$U = [\boldsymbol{u}_{\mathrm{InSAR}} \quad \boldsymbol{u}_{\mathrm{MAI}} \quad \cdots \quad \boldsymbol{u}_{\mathrm{InMAR}_n} \quad \boldsymbol{u}_{\mathrm{MAI}_m}] \tag{2}$$

where $\boldsymbol{u}_{\mathrm{InSAR}_n}$ and $\boldsymbol{u}_{\mathrm{MAI}_m}$ are the nth and mth unit vectors of the InSAR and MAI measurements, respectively. The unit InSAR vector is defined as follows:

$$\boldsymbol{u}_{\mathrm{InSAR}} = [\sin\theta\cos\phi \quad -\sin\theta\sin\phi \quad -\cos\theta]^{\mathrm{T}} \tag{3}$$

where $[\ ]^{\mathrm{T}}$ means the transpose of the vector, and θ and ϕ are the radar incidence and satellite track angles from the north, respectively, and the unit MAI vector can be defined as follows:

$$\boldsymbol{u}_{\mathrm{MAI}} = [\sin\theta \quad \cos\phi \quad 0]^{\mathrm{T}} \tag{4}$$

Finally, the 3D surface deformation can be generated by the least-squares solution as follows, where Σ is the covariance matrix of the InSAR and MAI measurements [8]:

$$\boldsymbol{d} = \left(U^{\mathrm{T}}\Sigma^{-1}U\right)^{-1} \cdot \left(U^{\mathrm{T}}\Sigma^{-1}\boldsymbol{r}\right) \tag{5}$$

The InSAR measurement contains both horizontal and vertical deformation components but fewer north components. However, the MAI measurements in the east and up directions have nearly no relation. In addition, the MAI geometries acquired from the ascending and descending orbits are in the opposite direction but similar. Thus, if one of the two MAI measurements is not good, one of the MAI measurements is not used to retrieve the northward deformation. Therefore, to optimally separate east, north, and vertical deformations, the total measurements should be greater than three, including at least two InSAR measurements from both ascending and descending orbits and one MAI measurement, respectively, as in Eq. (2).

4. Results

3D deformation retrieval using InSAR and MAI integration was applied to the 2016 Kumamoto earthquake to test the feasibility of precisely measuring 3D surface deformation via the improved InSAR and MAI integration in a large and complex deformation area. It is well known that the 2016 Kumamoto earthquake was generated along a right-lateral strike-slip fault. It has been reported that the earthquake-related deformation was approximately 2.1 m in the vertical direction and approximately 2.0 m in the horizontal direction [40,44].

Two ascending pairs and one descending co-seismic interferometric pair were acquired to analyze the 2016 Kumamoto earthquake (Table 1). Three wrapped differential interferograms were created via seven processing steps, as follows: ① azimuth common band filtering; ② offset parameter estimation; ③ slave SLC image resampling; ④ interferogram generation; ⑤ synthetic interferogram generation using the Shuttle Radar Topography Mission digital elevation model; ⑥ wrapped differential interferogram generation and multilooking using (15 × 12)-pixel looks in the azimuth and range directions; and ⑦ wrapped differential interferogram filtering with a kernel size of 32. Fig. 3 shows the wrapped differential interferograms of the ascending pairs 20151119_20160616 and 20160211_20160602 and the descending pair 20160307_20160418. The InSAR phase gradient is steep because a large co-seismic deformation exists, as shown in Fig. 3. The steepest deformation is seen near the fault zone (Fig. 3).

The interferometric phase in these areas could not be properly observed because it was not possible to unwrap the phase in the steep and complex deformation. To overcome this limitation, the multi-kernel offset tracking method was used to process the three pairs. A total of 16 offset measurements were obtained using 16 different kernel sizes from 32 × 32 to 256 × 256 pixels. The final offset measurement at each pixel was estimated using 3D median filtering with a kernel size of 3 × 3 × 16 pixels. The final range offset maps were converted from pixels to radians and then smoothed using the non-local (NL) means filter with a (11 × 11)-pixel kernel size to generate the wrapped residual interferogram. Consequently, the wrapped residual interferograms were easily and precisely unwrapped using the traditional minimum cost flow (MCF) algorithm [45].

Fig. 4 shows the unwrapped differential interferograms of the ascending pairs 20151119_20160616 and 20160211_20160602 and the descending pair 20160307_20160418. Notably, one fringe in Fig. 4 is different from that in Fig. 3. The one fringe in Fig. 4 corresponds to 4π. As seen in Fig. 4, the interferometric phase was properly unwrapped in the high fringe rate areas near the fault zone. The properly unwrapped phase was found even in areas that did not have any fringe patterns near the fault line. In these areas, the interferometric phase has no fringe pattern while the range offset has a valid measurement. This is because the deformation is complex and large in these areas, while the decorrelation factor is low. Thus, the measured interferometric phase is valid although it does not create any fringe patterns because of the low decorrelation. The results indicate that the large and complex deformation near the fault zone was well measured using the improved InSAR method. The measurement results were well matched in comparison with GPS-derived LOS deformation. The archived accuracies of the final interferograms were approximately 2.88, 1.96, and 1.90 cm for the asc1, asc2, and dsc pairs [41,44]. Hence, we consider that additional ionospheric correction was not essential.

To generate the MAI interferograms, ALOS-2 PALSAR-2 SLC images were Fourier-transformed in the azimuth direction and Doppler spectra were split into forward- and backward-looking bandwidths using the Hamming window. During this step, because the Doppler spectra were already applied using a windowing function, we first removed the applied window and then applied the split-band filtering to the Doppler spectra. Then, to generate the residual interferograms, we applied the full-aperture differential interferograms to hard filters, which were designed with kernel sizes of 256 × 256, 128 × 128, and 64 × 64 pixels. The hard-filtered differential interferograms were assumed to be noise-free interferograms; hence, we could create the forward- and backward-looking residual interferograms through phase subtraction between the hard-filtered interferogram and the forward- and backward-looking interferograms. After the forward- and backward-looking residual interferograms were slightly filtered

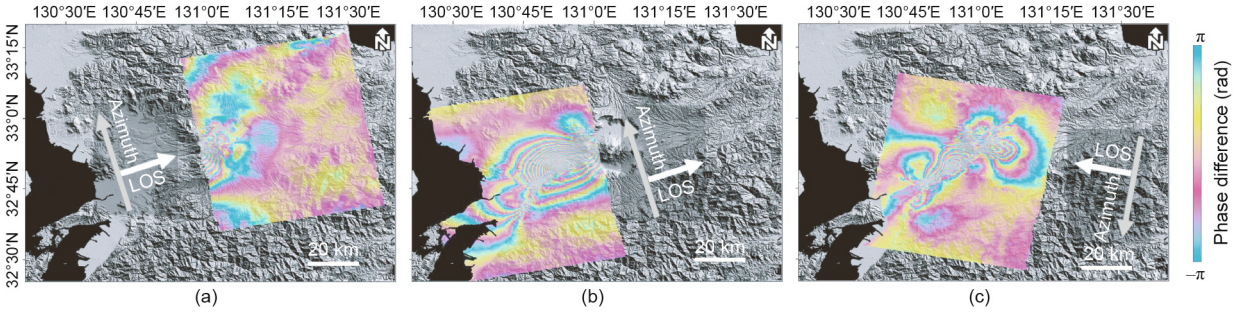

Fig. 3. Wrapped InSAR interferograms generated from the interferometric pairs of (a) 20151119_20160616, (b) 20160211_20160602, and (c) 20160307_20160418. 1 rad = 180°/π.

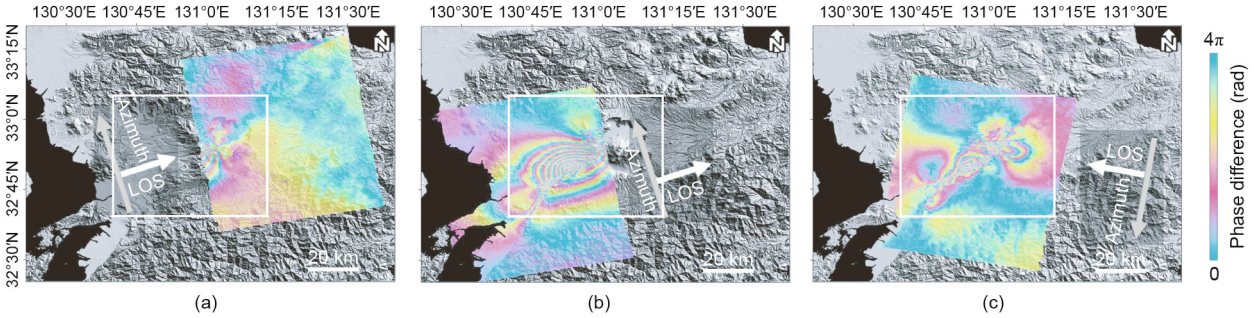

Fig. 4. Unwrapped InSAR interferograms created using the improved InSAR processor from the (a) 20151119_20160616, (b) 20160211_20160602, and (c) 20160307_20160418 interferometric pairs. White boxes show the coverage of 3D measurements.

using the Goldstein filter, the MAI interferogram was generated by the complex conjugate of the two residual interferograms. Because the MAI interferograms had topographic and flat-Earth phases, the phases were corrected using a method proposed in Ref. [23]. Some of the MAI interferograms had ionospheric effects, which should be mitigated; thus, we applied the directional filtering approach to the MAI interferograms. More details of the directional filtering can be found in Refs. [13,15,46,47].

Fig. 5 shows the MAI interferograms generated from the ascending pairs of 20151119_20160616 and 20160211_20160602 and the descending pair of 20160307_20160418. When the MAI interferograms in Fig. 5 were compared with the InSAR interferograms in Fig. 4, the MAI interferograms had a much lower spatial resolution because they were generated using sub-aperture processing. It is notable that one fringe in Fig. 5 corresponds to 0.2π. As seen in Fig. 5, the MAI phase was properly measured in the high fringe rate areas near the fault zone as well as in the areas that did not have any fringe patterns near the fault line. This is because the forward- and backward-looking residual interferograms have valid measurements because of the low decorrelation. The results indicate that the large and complex deformation near the fault zone was well measured using the improved MAI method. The achieved accuracies of the two ascending AT deformation measurements were approximately 8.13 and 9.87 cm (Figs. 5(a) and (b)), while the accuracy of the descending AT deformation was approximately 3.36 cm (Fig. 5(c)). The larger error in the former two measurements was because the ascending MAI interferograms included severe ionospheric distortion, as seen in Figs. 6(a) and (b). To mitigate the ionospheric distortion shown in Fig. 6(a), we iteratively applied a directional median filter with a rotation angle of 45° and a window kernel of 151 × 63 pixels in the along and cross ionospheric streak directions. In addition, a directional median filter with a rotation angle of 50° and a window kernel of 751 × 63 pixels was iteratively applied to the MAI interferogram shown in Fig. 6(b). More details of the ionospheric mitigation can be found in Refs. [13,46]. The mitigation of the ionospheric distortions via directional median filtering can be seen in Figs. 5(a) and (b). Through this mitigation, we improved the accuracies from

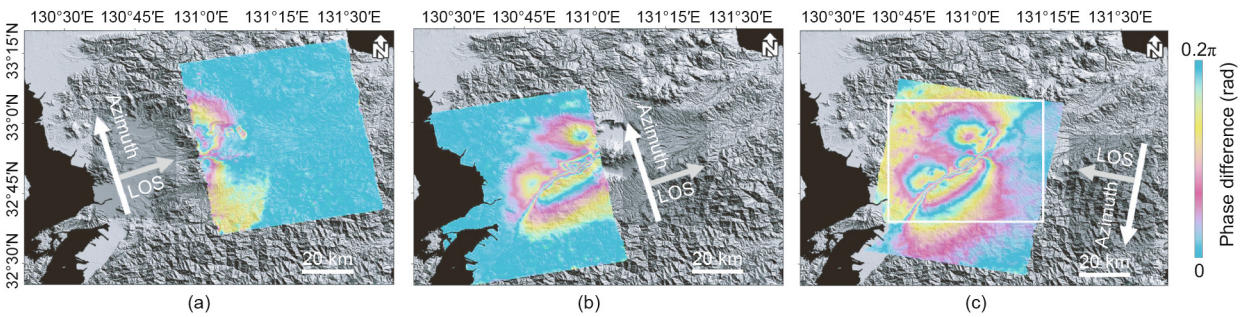

Fig. 5. Ionosphere-corrected MAI interferograms created using the improved MAI processor from the (a) 20151119_20160616, (b) 20160211_20160602, and (c) 20160307_20160418 interferometric pairs. White boxes show the coverage of 3D measurements.

approximately 52.29 and 47.55 cm to approximately 8.13 and 9.87 cm in the ascending pairs 20151119_20160616 and 20160211_20160602, respectively. Nevertheless, the accuracy of the ascending AT deformation was much lower than that of the descending AT deformation. Thus, the ascending AT deformation was not used to retrieve the 3D deformation field.

Interferometric decorrelation is a principal factor to estimate the measurement precision of InSAR and MAI interferograms. In particular, the MAI measurement precision is more sensitive to the decorrelation than the InSAR. Thus, the decorrelation factor needs to be considered before using MAI interferograms [26]. Spatial, temporal, thermal, and volume decorrelations are well known to be the decorrelation components [48]. Coherence can well describe the phase decorrelation and is usually utilized to estimate the theoretical error level [25,48]. As the coherence calculates the spatial stability of the phase signal, it can be underestimated in a high-gradient deformation area [41]. In other words, the coherence cannot be used to decide whether a valid deformation in a large and complex deformation area exists or not. It should be more carefully analyzed in large and complex deformation areas.

Fig. 7 shows the coherence map estimated from the descending forward-looking residual interferogram and the descending MAI interferogram masked by less than 0.5 coherence. The coherence was calculated using a 5 × 5-pixel moving window. The coherence values in most areas were near 1.0; coherence values from 0.5 to 0.7 were observed near fault lines. As shown in Fig. 7(b), the low coherence values were mainly distributed in the very steep deformation areas. In these areas, the calculated coherence values could not be used to estimate the MAI precision; hence, we could not decide whether the deformation measurement in these areas was valid using the coherence or not. Therefore, offset tracking information was additionally used to decide upon a valid measurement.

Fig. 8 shows the 2016 Kumamoto earthquake 3D surface deformation field created by integrating the improved InSAR and MAI methods. We used the LOS deformation maps measured from the two ascending pairs and one descending pair and the AT

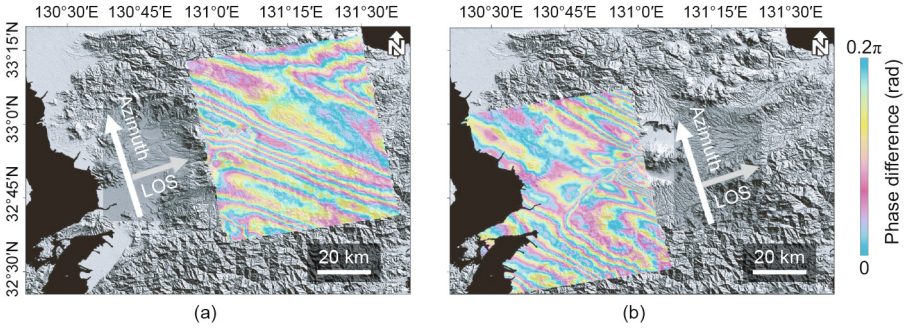

Fig. 6. MAI interferograms before the ionospheric correction: (a) 20151119_20160616; (b) 20160211_20160602.

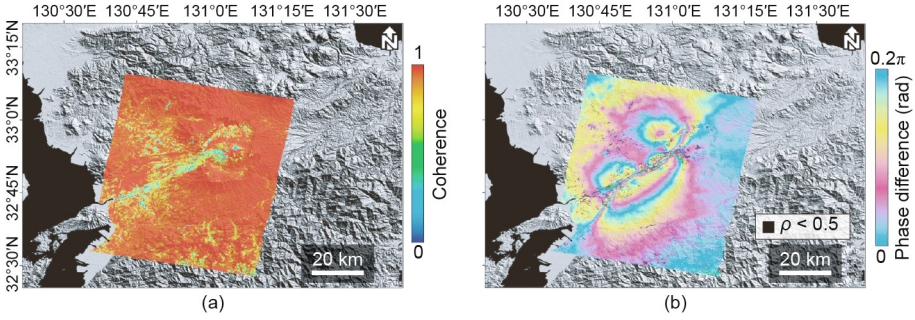

Fig. 7. (a) Coherence map of a descending forward-looking residual interferogram; (b) threshold map of coherence by a criterion of 0.5 on the descending MAI interferogram. Black pixels indicate an area of lower coherence than 0.5; ρ means the coherence value.

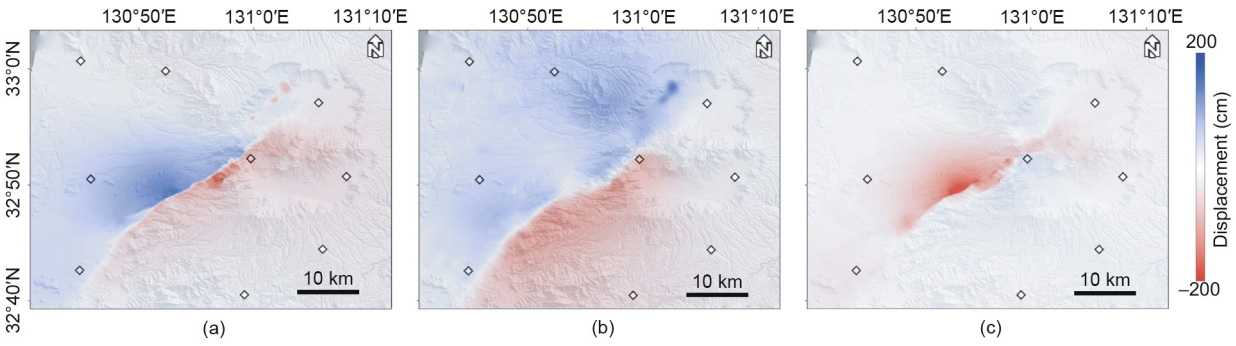

Fig. 8. 3D surface deformation field of the 2016 Kumamoto earthquake created using the integrated InSAR and MAI method: (a) eastward, (b) northward, and (c) upward deformations. Colored diamonds on (a)–(c) indicate the surface deformation from the GPS stations.

deformation map measured from the descending pair. As shown in Fig. 8, the 3D deformation field was well retrieved, even given the large and complex deformation. The positive and negative maximum deformations were approximately 1.78 and −1.81 m in the east direction (Fig. 8(a)), approximately 1.57 and −1.04 m in the north direction (Fig. 8(b)), and approximately 2.49 and −0.56 m (Fig. 8(c)) in the up direction, respectively.

Fig. 9 shows the horizontal deformation vector field calculated by combining the eastward and northward deformations. As shown in Fig. 9, the base map of the vector field originates from the upward deformation. The vector field shows that the 2016 Kumamoto earthquake was generated along a right-lateral strike-slip fault. Moreover, approximately 2.49 m of uplift was observed on the west part of the fault while approximately 0.56 m of subsidence was measured on the east part of the fault. This means that the 2016 Kumamoto earthquake was characterized by both right-lateral strike-slip and normal fault motions.

To test the achieved accuracy of the 3D surface deformation field derived using InSAR and MAI integration, we compared the SAR-derived deformation with the *in situ* GPS deformation data acquired from 11 stations (Fig. 10). The SAR-derived deformation was extracted from the 11 station positions using the cubic interpolation method. The root-mean-square errors (RMSEs) between the SAR-derived and *in situ* GPS deformations were approximately 2.96, 3.75, and 2.86 cm in the east, north, and up directions, respectively. The agreement between the InSAR and MAI integration and the *in situ* GPS measurements of the northward deformation field was worse than those of the eastward and upward deformation fields because the LOS deformation using InSAR is more precise than the AT deformation using MAI.

From the results, we can conclude that the precise 3D deformation field was retrieved in a large and complex deformation area using the improved InSAR and MAI integration, as long as the decorrelation factor was low. To assess whether the decorrelation is low in a complex and large deformation area, the offset tracking method can be used. If a valid offset measurement can be obtained from the area, it is possible to obtain a valid 3D deformation measurement because of the high correlation. Otherwise, the measured 3D deformation in the area is not valid. Precisely measured 3D deformation allows for a better understanding of geological events such as earthquakes and volcanic eruptions.

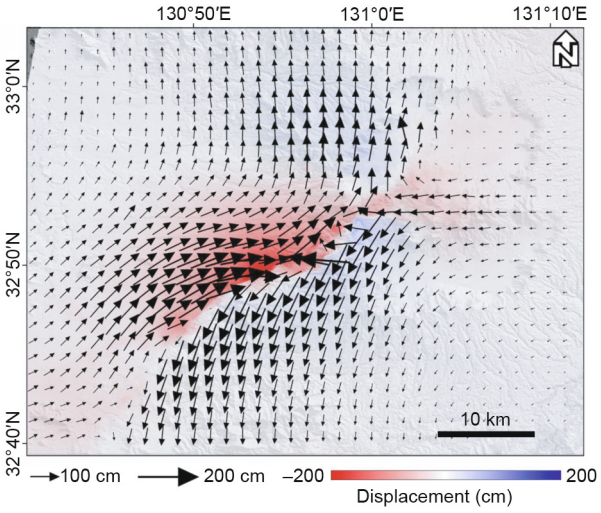

Fig. 9. Horizontal deformation vector field calculated by combining the eastward and northward deformations. The base map of the vector field is the upward deformation.

5. Conclusions

We tested the feasibility of obtaining precise 3D deformation measurements in large and complex deformation areas via the integration of the improved InSAR and MAI methods. To do so, the 2016 Kumamoto earthquake 3D surface deformation field was observed using the integration method. The 2016 Kumamoto earthquake-related deformation was large and complex near the fault line; hence, precise 3D surface deformation retrieval had not been yet performed using InSAR and MAI integration. Two ascending pairs and one descending ALOS-2 PALSAR-2 interferometric pairs were used in this study for the 3D deformation retrieval.

Conventional InSAR processing was applied to the SLC interferometric pairs to create three wrapped differential interferograms, and the multi-kernel offset tracking method was used to generate three range offset maps. The range offset tracking method well measured the complex and large deformation field near the fault line. This means that the decorrelation was low near the fault line. Thus, we attempted to unwrap the three differential interferograms using the offset-based unwrapping approach; the unwrapping approach was well applied to the three interferograms. This indicates that the large and complex deformation near the fault zone was successfully observed using the unwrapping approach based on the offset measurement. Three MAI interferograms were generated using forward- and backward-looking residual interferograms. They well measured the complex and large deformation field near the fault line because of the low decorrelation. Two ascending MAI interferograms had severe ionospheric distortion, which was corrected. However, the RMSEs of the corrected ascending MAI interferograms were three times lower than that of the

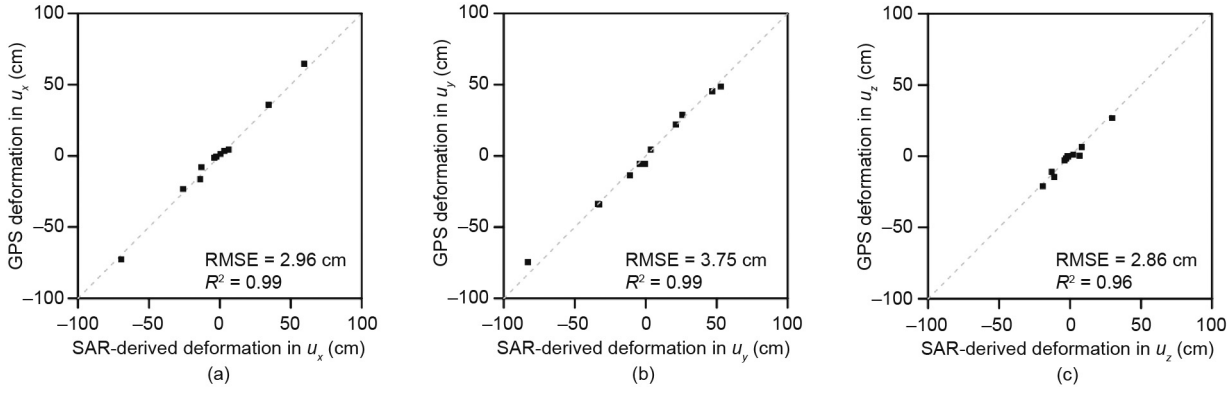

Fig. 10. Comparison of SAR-derived deformation with the *in situ* GPS deformation in the (a) east (u_x), (b) north (u_y), and (c) up (u_z) directions. RMSE: the root mean square errors.

descending MAI interferogram. Thus, the two ascending MAI interferograms were not used to retrieve the 3D deformation.

The 2016 Kumamoto earthquake 3D surface deformation field was retrieved from the three unwrapped differential interferograms and the descending MAI interferograms. The 3D deformation map clearly shows that the 3D deformation field was well retrieved, even in the large and complex deformation area. It is clear from the 3D deformation map that the 2016 Kumamoto earthquake was characterized by both right-lateral strike-slip and normal fault motions. A performance test of the 3D deformation field was performed by comparing the SAR-derived result with the *in situ* GPS deformation. The RMSEs in the east, north, and up directions were approximately 2.96, 3.75, and 2.86 cm, respectively. These results prove that a precise 3D deformation field was retrieved in this large and complex deformation area using the improved InSAR and MAI integration, as long as the decorrelation was low. Precisely measured 3D deformation allows for a better understanding of geological events such as earthquakes and volcanic eruptions.

Acknowledgements

This study was funded by the Korea Meteorological Administration Research and Development Program (KMI2017-9060) and the National Research Foundation of Korea funded by the Korea government (NRF-2018M1A3A3A02066008). In addition, the ALOS-2 PALSAR-2 data used in this study are owned by the Japan Aerospace Exploration Agency (JAXA) and were provided through the JAXA's ALOS-2 research program (RA4, PI No. 1412). The GPS data were provided by the Geospatial Information Authority of Japan.

Compliance with ethics guidelines

Won-Kyung Baek and Hyung-Sup Jung declare that they have no conflict of interest or financial conflicts to disclose.

References

[1] Biggs J, Amelung F, Gourmelen N, Dixon TH, Kim SW. InSAR observations of 2007 Tanzania rifting episode reveal mixed fault and dyke extension in an immature continental rift. Geophys J Int 2009;179(1):549–58.
[2] Wei M, Sandwell D, Fialko Y, Bilham R. Slip on faults in the Imperial Valley triggered by the 4 April 2010 Mw 7.2 El Mayor–Cucapah earthquake revealed by InSAR. Geophys Res Lett 2011;38(1):L01308.
[3] Jung HS, Hong SM. Mapping three-dimensional surface deformation caused by the 2010 Haiti earthquake using advanced satellite radar interferometry. PLoS ONE 2017;12(11):e0188286.
[4] Jo MJ, Jung HS, Yun SH. Retrieving precise three-dimensional deformation on the 2014 M6.0 South Napa earthquake by joint inversion of multi-sensor SAR. Sci Rep 2017;7(1):5485.
[5] Jo MJ, Jung HS, Chae SH. Advances in three-dimensional deformation mapping from satellite radar observations: application to the 2003 Bam earthquake. Geomatics Nat Hazards Risk 2018;9(1):678–90.
[6] Lee WJ, Lu Z, Jung HS, Ji L. Measurement of small co-seismic deformation field from multi-temporal SAR interferometry: application to the 19 September 2004 Huntoon Valley earthquake. Geomatics Nat Hazards Risk 2017;8(2):1241–57.
[7] Lu Z, Dzurisin D, Biggs J, Wicks C Jr, McNutt S. Ground surface deformation patterns, magma supply, and magma storage at Okmok volcano, Alaska, from InSAR analysis: 1. intereruption deformation, 1997–2008. J Geophys Res 2010;115:B00B02.
[8] Jung HS, Lu Z, Won JS, Poland MP, Miklius A. Mapping three-dimensional surface deformation by combining multiple-aperture interferometry and conventional interferometry: application to the June 2007 eruption of Kilauea volcano, Hawaii. IEEE Geosci Remote Sens Lett 2011;8(1):34–8.
[9] Jo MJ, Jung HS, Won JS. Measurement of precise three-dimensional volcanic deformations via TerraSAR-X synthetic aperture radar interferometry. Remote Sens Environ 2017;192:228–37.
[10] Lee WJ, Lu Z, Jung HS, Park SC, Lee DK. Using a refined SBAS algorithm to determine surface deformation in the Long Valley caldera and its surroundings from 2003–2010. Korean J Remote Sens 2018;34(1):101–15.
[11] Qu F, Lu Z, Poland M, Freymueller J, Zhang Q, Jung HS. Post-eruptive inflation of Okmok volcano, Alaska, from InSAR, 2008–2014. Remote Sens 2015;7(12):16778–94.
[12] Gray L. Using multiple RADARSAT InSAR pairs to estimate a full three-dimensional solution for glacial ice movement. Geophys Res Lett 2011;38(5):L05502.
[13] Chae SH, Lee WJ, Jung HS, Zhang L. Ionospheric correction of L-band SAR offset measurements for the precise observation of glacier velocity variations on Novaya Zemlya. IEEE J Sel Top Appl Earth Obs Remote Sens 2017;10(8):3591–603.
[14] Boncori JPM, Andersen ML, Dall J, Kusk A, Kamstra M, Andersen SB, et al. Intercomparison and validation of SAR-based ice velocity measurement techniques within the Greenland ice sheet CCI project. Remote Sens 2018;10(6):929.
[15] Baek WK, Jung HS, Chae SH, Lee WJ. Two-dimensional velocity measurements of Uvêrsbreen glacier in Svalbard using TerraSAR-X offset tracking approach. Korean J Remote Sens 2018;34(3):495–506.
[16] Choi JK, Won JS, Lee S, Kim SW, Kim KD, Jung HS. Integration of a subsidence model and SAR interferometry for a coal mine subsidence hazard map in Taebaek, Korea. Int J Remote Sens 2011;32(23):8161–81.
[17] Zhang L, Ding X, Lu Z, Jung HS, Hu J, Feng G. A novel multi-temporal InSAR model for joint estimation of deformation rates and orbital errors. IEEE Trans Geosci Remote Sens 2014;52(6):3529–40.
[18] Choi JH, Kim SW. Comparison of observation performance of urban displacement using ALOS-1 L-band PALSAR and COSMO-SkyMed X-band SAR time series images. Korean J Remote Sens 2018;34(2):283–93.
[19] Baek WK, Jung HS, Jo MJ, Lee WJ, Zhang L. Ground subsidence observation of solid waste landfill park using multi-temporal radar interferometry. Int J Urban Sci 2019;23(3):406–21.
[20] Lu Z, Kwoun O. Radarsat-1 and ERS InSAR analysis over southeastern coastal Louisiana: implications for mapping water-level changes beneath swamp forests. IEEE Trans Geosci Remote Sens 2008;46(8):2167–84.
[21] Hong SH, Wdowinski S. A review on monitoring the Everglades wetlands in the southern Florida using space-based synthetic aperture radar (SAR) observations. Korean J Remote Sens 2017;33(4):377–90.
[22] Bechor NBD, Zebker HA. Measuring two-dimensional movements using a single InSAR pair. Geophys Res Lett 2006;33(16):L16311.
[23] Jung HS, Won JS, Kim SW. An improvement of the performance of multiple-aperture SAR interferometry (MAI). IEEE Trans Geosci Remote Sens 2009;47(8):2859–69.
[24] Jung HS, Lu Z, Zhang L. Feasibility of along-track displacement measurement from Sentinel-1 interferometric wide-swath mode. IEEE Trans Geosci Remote Sens 2013;51(1):573–8.
[25] Jung HS, Lee WJ, Zhang L. Theoretical accuracy of along-track displacement measurements from multiple-aperture interferometry (MAI). Sensors 2014;14(9):17703–24.
[26] Jung HS, Yun SH, Jo MJ. An improvement of multiple-aperture SAR interferometry performance in the presence of complex and large line-of-sight deformation. IEEE J Sel Top Appl Earth Obs Remote Sens 2015;8(4):1743–52.
[27] Jung HS, Lu Z, Shepherd A, Wright T. Simulation of the SuperSAR multi-azimuth synthetic aperture radar imaging system for precise measurement of three-dimensional Earth surface displacement. IEEE Trans Geosci Remote Sens 2015;53(11):6196–206.
[28] Jo MJ, Jung HS, Won JS, Poland MP, Miklius A, Lu Z. Measurement of slow-moving along-track displacement from an efficient multiple-aperture SAR interferometry (MAI) stacking. J Geod 2015;89(5):411–25.
[29] Jo MJ, Jung HS, Won JS, Lundgren P. Measurement of three-dimensional surface deformation by COSMO-SkyMed X-band radar interferometry: application to the March 2011 Kamoamoa fissure eruption, Kīlauea volcano, Hawai'i. Remote Sens Environ 2015;169:176–91.
[30] Jo MJ, Jung HS, Won JS. Detecting the source location of recent summit inflation via three-dimensional InSAR observation of Kīlauea volcano. Remote Sens 2015;7(11):14386–402.
[31] Morishita Y, Kobayashi T, Yarai H. Three-dimensional deformation mapping of a dike intrusion event in Sakurajima in 2015 by exploiting the right- and left-looking ALOS-2 InSAR. Geophys Res Lett 2016;43(9):4197–204.
[32] Hu J, Ding XL, Zhang L, Sun Q, Li ZW, Zhu JJ, et al. Estimation of 3-D surface displacement based on InSAR and deformation modeling. IEEE Trans Geosci Remote Sens 2017;55(4):2007–16.
[33] Hu J, Li ZW, Ding XL, Zhu JJ, Zhang L, Sun Q. 3D coseismic displacement of 2010 Darfield, New Zealand earthquake estimated from multi-aperture InSAR and D-InSAR measurements. J Geod 2012;86(11):1029–41.
[34] Boncori JPM, Papoutsis I, Pezzo G, Tolomei C, Atzori S, Ganas A, et al. The February 2014 Cephalonia earthquake (Greece): 3D deformation field and source modeling from multiple SAR techniques. Seismol Res Lett 2014;86(1):1–14.
[35] Wang X, Liu G, Yu B, Dai K, Zhang R, Chen Q, et al. 3D coseismic deformations and source parameters of the 2010 Yushu earthquake (China) inferred from DInSAR and multiple-aperture InSAR measurements. Remote Sens Environ 2014;152:174–89.
[36] Wang X, Liu G, Yu B, Dai K, Zhang R, Ma D, et al. An integrated method based on DInSAR, MAI and displacement gradient tensor for mapping the 3D coseismic deformation field related to the 2011 Tarlay earthquake (Myanmar). Remote Sens Environ 2015;170:388–404.
[37] Grandin R, Klein E, Métois M, Vigny C. Three-dimensional displacement field of the 2015 Mw 8.3 Illapel earthquake (Chile) from across- and

along-track Sentinel-1 TOPS interferometry. Geophys Res Lett 2016;43 (6):2552–61.
[38] Hu J, Li ZW, Li J, Zhang L, Ding XL, Zhu JJ, et al. 3-D movement mapping of the alpine glacier in Qinghai–Tibetan Plateau by integrating D-InSAR, MAI and offset-tracking: case study of the Dongkemadi glacier. Global Planet Change 2014;118:62–8.
[39] Gourmelen N, Kim SW, Shepherd A, Park JW, Sundal AV, Björnsson H, et al. Ice velocity determined using conventional and multiple-aperture InSAR. Earth Planet Sci Lett 2011;307(1–2):156–60.
[40] Himematsu Y, Furuya M. Fault source model for the 2016 Kumamoto earthquake sequence based on ALOS-2/PALSAR-2 pixel-offset data: evidence for dynamic slip partitioning. Earth Planets Space 2016;68(1):169.
[41] Baek WK, Jung HS, Chae SH. Feasibility of ALOS2 PALSAR2 offset-based phase unwrapping of SAR interferogram in large and complex surface deformations. IEEE Access 2018;6:45951–60.
[42] Chae SH, Lee WJ, Baek WK, Jung HS. An improvement of the performance of SAR offset tracking approach to measure optimal surface displacements. IEEE Access 2019;7:131627–37.
[43] Wright TJ, Parsons BE, Lu Z. Toward mapping surface deformation in three dimensions using InSAR. Geophys Res Lett 2004;31(1):L01607.
[44] Baek WK, Jung HS, Chae SH. Precise three-dimensional mapping of the 2016 Kumamoto earthquake through the integration of SAR interferometry and offset tracking. In: Proceedings of the 2017 IEEE International Geoscience and Remote Sensing Symposium; 2017 Jul 23–28; Fort Worth, TX, USA. New York: IEEE; 2017. p. 3822–3.
[45] Costantini M. A novel phase unwrapping method based on network programming. IEEE Trans Geosci Remote Sens 1998;36(3):813–21.
[46] Baek WK, Jung HS. Precise measurements of the along-track surface deformation related to the 2016 Kumamoto earthquakes via ionospheric correction of multiple-aperture SAR interferograms. Korean J Remote Sens 2018;34(6):1489–501.
[47] Lee WJ, Jung HS, Chae SH, Baek WK. Enhancement of ionospheric correction method based on multiple aperture interferometry. Korean J Remote Sens 2015;31(2):101–10.
[48] Zebker HA, Villasenor J. Decorrelation in interferometric radar echoes. IEEE Trans Geosci Remote Sens 1992;30(5):950–9.